Excitonic properties of clustered-*P*1 borophene

Vaishnavi Vishnubhotla and Santanu Mahapatra*
Nanoscale Device Research Laboratory, Department of Electronics Systems Engineering, Indian Institute of Science, Bangalore 560012, India

Sitangshu Bhattacharya†
Electronic Structure Theory Group, Department of Electronics and Communication Engineering, Indian Institute of Information Technology-Allahabad, Uttar Pradesh 211015, India

(Received 15 August 2023; revised 16 October 2023; accepted 5 November 2023; published 4 December 2023)

Using rigorous *ab initio* calculations of many-body electron-electron, electron-phonon, electron-hole, and exciton-phonon couplings, we demonstrate that the recently discovered semiconducting phase, clustered-P1 borophene, can exhibit an optical gap of 0.74 eV and possesses a substantial binding energy of 1.5 eV at room temperature. Additionally, it features a significantly faster nonradiative recombination rate at room temperature. The profound impact of dynamical self-energies originating from pure electron-phonon interactions results in a noteworthy zero-point renormalization of the quasiparticle direct and indirect gaps, leading to large shifts of 73 and 91 meV, respectively. We demonstrate strong, incoherent interactions between electrons and holes with lattice vibrations, resulting in a significant redshifting of the absorption spectrum at 0 K. The pivotal phonon modes responsible for shaping the lowest bound exciton originates from the spectral range of 350–950 cm^{-1} and also exhibits resilience against temperature variations. Notably, the room temperature nonradiative lifetime of the lowest bound exciton is found to be significantly smaller (∼40 fs) compared to its intrinsic radiative lifetime (∼0.6 ns). These remarkable outcomes collectively suggest that clustered-P1 borophene is a formidable contender for the development of near-ultraviolet optoelectronic devices.

DOI: 10.1103/PhysRevB.108.245107

I. INTRODUCTION

Atomically thin materials have emerged as an excellent platform to understand various strongly correlated optical processes at nonzero temperatures using tabletop experiments. The absence of an inversion symmetry (i.e., noncentrosymmetric crystalline structure) and the presence of time-reversal symmetry (i.e., $[E(\mathbf{K}\uparrow) = E(\mathbf{K}'\downarrow)]$) in conventional atomic layers like transition metal dichalcogenides (TMDCs) has resulted in a strong spin-orbit valence splitting and spin-valley momenta coupling [1–3]. Particularly, an exciton is a boson-like quasiparticle and is the fundamental collective excitation in a weak dielectric. Being a Coulombically bounded electron-hole pair, an exciton can be viewed as a two-body correlated state of affair. Generally, photon frequencies above the quasiparticle gap should facilitate the excitation of an electron from the valance band to the conduction band. However, in the presence of strong long-range dynamic correlation, the absorption instead takes place below this gap, suggesting the existence of distinct excitonic states similar to the midgap states in a defected crystal. A variety of interesting excitonic activities because of such conditional symmetries are seen, for example, in the two-dimensional (2D) TMDCs that result in valley polarization [4], giant spin-valley coupling [5], Zeeman effect [6], momentum forbidden dark excitonic states [7–9], giant spin-orbit coupling [10,11], and Davydov splitting [12]. Strong electron-hole correlation in these monolayers are clearly observed from their neutral excitonic fingerprints such as the binding energy (BE) and FWHM (full width at half maximum) linewidths. For example, a large room temperature (RT) BE in 2D TMDCs is reported in the range of 0.37–0.929 eV [10,13–15] on an exfoliated Si/SiO_2 substrate. In other contemporary 2D materials like black phosphorus (BP) and hexagonal boron nitride (h-BN), the RT-BE are reported as 0.139 eV [16] and 1.9 eV [17] on a PDMS (polydimethylsiloxane), and epitaxially grown over a graphite substrate, respectively. While the FWHM linewidths in the former are reported between 10–50 meV at 4–300 K [18,19], their encapsulation with h-BN further dramatically seem to reduces these by one order [20–22]. The linewidths in the case of monolayer h-BN and few-layer BP are reported in the range of 32(10 K)–38(300 K) meV [17] and 20 meV [16], respectively.

A recent member of the monoelemental 2D material family, borophene, has drawn a lot of interest because of its ultralow molar mass and fascinating chemistry, which is the result of exceptional polymorphism. The origin of the 2D network of boron atoms goes back to 1997, when Boustani [23] proposed the Aufbau principle to build 2D boron sheets by merging two basic structural units, the pentagonal pyramid unit B6 and the hexagonal pyramid unit B7. However, bulk boron, unlike graphite, doesn't possess a layered structure, and hence the experimental realization of borophene occurred only in 2015 [24]. In contrast to graphene again, that study and subsequent experiments [25,26] found borophene in various

*santanu@iisc.ac.in
†sitangshu@iiita.ac.in

 ©2023 American Physical Society

polymorphs (α, β_{12}, χ_3, and honeycomb), which are made up of hollow hexagons and triangular lattices [27]. It is, however, remarkable to note that all these synthesized polymorphs of borophene are found to be metallic although bulk boron is semiconducting in nature. As a result, despite substantial research into borophene uses such as energy storage [28–30], catalysis [31,32], sensors [33,34], and so on, it has not been found to be suitable for optoelectronics. Using a genetic algorithm-based structure finding technique, an allotrope of 2D boron called clustered-P1 (CP1) has been discovered recently [35], which is reported to be very close to the global minimum of the energy surface (0.07 eV/atom higher). More notably, the mild-indirect band gap of CP1 borophene was found to be 1.08 eV, which is very close to that of bulk silicon. Studies of phonon dispersion and beyond RT *ab initio* molecular dynamics simulations provide more evidence of its exceptional dynamic and structural stability. Such exciting features of CP1 motivate us to study its excitonic properties for possible application of borophene in optoelectronic devices.

Here, we present a detailed theory for temperature-dependent optical processes in CP1 borophene. Fully *ab initio* computations based on the many-body perturbation theory (MBPT) of the Bethe-Salpeter equation (BSE) are the most reliable approach for understanding exciton-driven linear and nonlinear optical properties from bulk materials to atomically thin layers [9,36–42], including comparisons with quantum Monte Carlo calculations [43]. We therefore employ a rigorous *ab initio* calculation that simultaneously considers the accurate description of electron-electron, electron-hole, electron-phonon, and exciton-phonon interactions to describe light absorption in the presence of lattice vibrations. As experiments are always performed at nonzero temperatures, a theory considering temperature effects on optical spectrum is a more realistic approach to investigate excitonic energies and lifetimes. However, to date, only a few such BSE calculations exist [44–52], confirming the necessity of additional electron-phonon coupling, which is fundamentally required in exciton development in atomic layers. Hence, using this nontrivial approach, we demonstrate that CP1 borophene exhibits a larger fundamental exciton binding energy of 1.5 eV with a linewidth of 51 meV at RT. The major exciton-phonon couplings occur between the midacoustic to lower optical zone of the phonon dispersion, suggesting a strong exciton phonon interaction that dominates within the 0–800 K temperature range. Interestingly, we find that the intrinsic excitonic radiative lifetimes are in subnanoseconds at RT (∼0.6 ns), where the nonradiative ones are in femtoseconds (∼40 fs). These outcomes are discussed in the Results and Discussion section. In addition, the Supplemental Material (SM) [53] (see also references) contains the methodologies and all the necessary convergence figures used in this paper.

II. RESULTS AND DISCUSSION

A. Ground-state energies and thermal stability

Ab initio density functional theory (DFT) based QUANTUM ESPRESSO open source code [58] is used to calculate all the ground-state energies (see the SM [53] for methodologies).

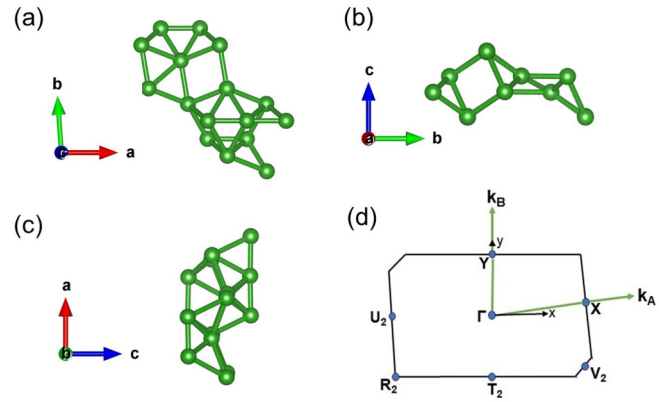

FIG. 1. (a)–(c) A fully relaxed structure. (d) The Brillouin zone of CP1 borophene primitive cell.

Once the structure is relaxed, the in-plane cell dimensions a and b obtained are 3.17 and 4.49 Å, respectively, and are shown in Figs. 1(a)–1(c). Since this CP1 structure does not have any crystalline symmetry, we therefore show the full Brillouin zone (BZ) route in Fig. 1(d). The ground - calculations show that the major contribution near the band gap comes from the two most important p_y and p_z orbitals (see Fig. S1 in the SM). The partial density of states (p-DOS) projected on the dispersion shows that the contribution from the s and p_x orbitals is insignificant near the conduction band minimum (CBM) and valence band maximum (VBM). Instead, the bands near the gap are mainly occupied by electrons from the p_z and p_y orbitals. The VBM is mainly populated by the p_z orbital electrons, while the CBM has a mixed occupancy from both the p_y and p_z orbitals. We find that both these top and bottom conduction bands are located near **X**, between the Γ-**X** direction. However, they are slightly shifted in momentum. This is depicted in Fig. 2. Additionally, there is a slight degeneracy of the conduction band at U_2 (for example, see Fig. S1 in the SM [53]), which, however, does not significantly influence optical transitions. Nevertheless, we find that the indirect and direct gaps are about 0.75 and 0.79 eV, respectively. We also report here the thermodynamic stability of CP1 borophene. We found a large formation energy of about −5.98 eV/atom with respect to an isolated boron atom, which suggests the stable existence of the freestanding configuration as a monolayer. However, the lattice dynamic stability, as shown in Fig. 3(a), is slightly weak at the zone center, indicating a small instability. This suggests that the exfoliation process might not be a suitable method for producing this phase of borophene. In any case, we should not rule out the possibility of obtaining a suitable substrate, such as encapsulation or wafer-grown samples, to ensure that all electronic and phononic branches remain unperturbed. As a summary, we list all the bare energies and lattice constants in Table I.

B. Effect of electron-phonon self-energies on electronic band structures

Figures 3(a) and 3(b) show the lattice vibration dispersion and the corresponding DOS, where all branches are infrared active. A careful inspection shows that there are slightly neg-

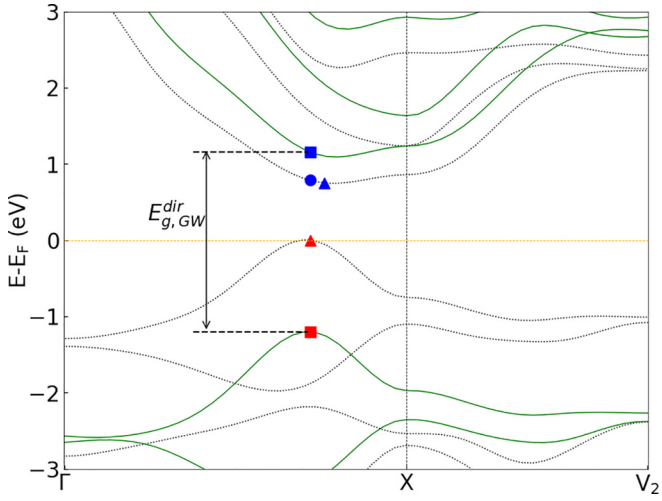

FIG. 2. Ground-state electronic band structure of CP1 borophene (dotted curve). The solid green curve represents the G_0W_0 quasiparticle electronic band structure. The symbols are the locations of valence (red) and conduction states (blue). The indirect bare-gap between symbols ▲-▲ is almost 0.75 eV. The direct bare-gap between symbols ●-▲ is almost 0.79 eV. The top of the ground state valence band is the reference 0 eV level. The G_0W_0 quasiparticle direct-gap between symbols ■-■ is about 2.34 eV.

ative frequencies in the out-of-plane and in-plane modes near the zone center Γ, which may give rise to small dynamic instability. However, such frequencies could also be due to the finite phonon grid sampling. Overall, the branches in the dispersion can be grouped between 300–500 cm^{-1} in the midacoustic zone, 600–900 cm^{-1} in the lower optical mode and at about 1450 cm^{-1} with the complicated torsional optical out-of-plane mode. The corresponding atomic vibrations in the midacoustic and lower optical zones are influenced by a complicated mixture of both in-plane and out-of-plane torsional motions. The phonon occupancy is clearly visible in the corresponding phonon DOS, where the lower acoustic branches have small phonon populations. The major density comes from the midacoustic zone between 300–500 cm^{-1}. Additionally, one can observe that within the zone of 1000–1400 cm^{-1}, a large phonon band gap exists with minor populations indicated by small peaks.

CP1 borophene is a lightweight material, and hence the atoms are expected to vibrate more with increasing temperatures. Therefore, the electron-phonon interactions in this case should have a profound effect on the band-gap renormalization and hence excitonic lifetimes. It is well understood now

TABLE I. Electronic *ab initio* energy of CP1 borophene. a, b, and z are the in-plane cell dimensions and buckling height, respectively. E_{form} is the formation energy per atom, ZPM is the zero-point gap, D=direct and I=indirect.

a (Å)	b (Å)	z (Å)	Indirect gap (eV)	Direct gap (eV)	E_{form} (eV/atom)	ZPM (meV)
3.17	4.49	2.51	0.75 (DFT)	0.79 (DFT) 2.34 (G_0W_0)	−5.98	73 (D) 91 (I)

from the dynamic Heine, Allen, and Cardona [59,60] (HAC theory) that the presence of such interactions significantly modifies the ground-state electronic energies by broadening them [44,45,61]. This is contrary to the case of a generic frozen atom (FA) picture, where the atoms are assumed to be fixed in space and the eigenenergies are completely real. However, such a picture does not agree with the Heisenberg's uncertainty principle, which prohibits the accurate measurement of position and momentum simultaneously. Hence, the presence of intrinsic spatial quantum uncertainty makes the atoms vibrate even at absolute zero Kelvin. This is known as zero-point motion (ZPM), where the electronic energies acquire a finite broadening at zero Kelvin. Such broadening are fundamental and are verified in materials like diamond [62,63], BN, LiF, and MgO [64], as well as in polymers [45], where they are comparable to the corresponding electron-electron correlational energies. These corrections are also found to be significant in the case of 2D materials like MoS_2 [46], WSe_2 [48], and h-BN [49,65], and are responsible for the red or blueshifting of the optical absorption spectrum. We therefore extend such corrections in CP1 borophene to check how strong the electron-phonon interactions are.

Figure 4(a) shows the energy corrections due to electron-phonon interactions on the FA electronic states. The real part of the difference reveals the actual corrections stemming from the Fan and Debye-Waller (DW) self-energies [44,45,61] both below and above the Fermi level. In Fig. 4(b), the corresponding linewidth is depicted at various temperatures, showing significantly large deviations. Since the linewidths are proportional to the electronic DOS, we have also included the same plot to understand their variations along the energy DOS. It is evident that these corrections are substantial, even when compared to the corresponding electron-electron correlational linewidths (indicated by black dots). This underscores the significance of electron-phonon interactions in CP1 borophene when describing optical processes.

The spectral function at three different temperatures of the electron-phonon correlated state is shown in Figs. 5(a)–5(c) at ▲ of the VBM and at ● and ▲ of the conduction state, respectively. The impact of renormalization is evident in the form of Lorentzian peak shifts away from their respective bare energy values. At lower temperatures, the peaks are sharp, indicating weaker electron-phonon correlations. With increasing temperature, electrons become more responsive to the heightened lattice vibrations, resulting in broader peaks. Further temperature increases lead to asymmetric and diminished peaks, signifying intensified interactions and a reduced electronic lifetime in the corresponding states. These quasiparticle characteristics can be understood through the dimensionless renormalization weight factor, Z [44], which ranges between 0 and 1. At 0 K, the valence Z is approximately 96%, signifying a genuine quasiparticle state. However, as the temperature rises, Z decreases to around 81%, indicating a higher degree of interaction. Similar observations are made for the two conduction states depicted in Figs. 5(b) and 5(c). We also note here the spectral shifts, both red and blue, with changing temperatures. The zero-point renormalization can be determined by the total reduction in the band gap at 0 K. Specifically, at 0 K, the valence spectral function experiences a blueshift of approximately 6 meV. In the case of the conduction state at

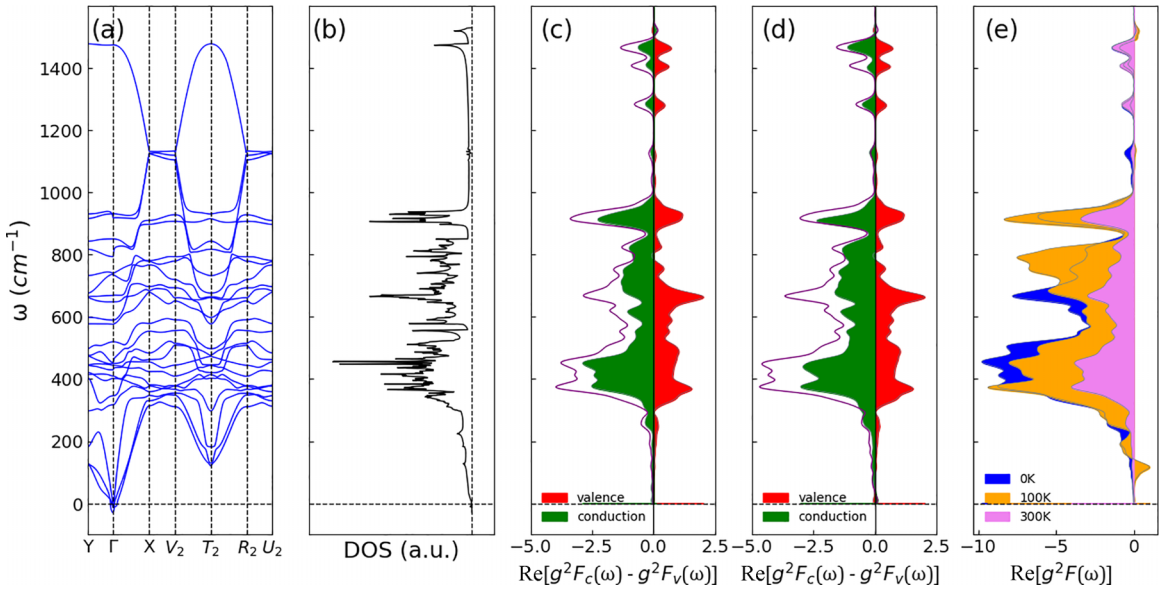

FIG. 3. (a) Lattice vibration dispersion and (b) phonon density of states of CP1 borophene along the Brillouin zone (BZ). (c) The difference of the real part of the electronic Eliashberg function $\mathrm{Re}[g^2F^c_{n\mathbf{k}}(\omega) - g^2F^v_{n\mathbf{k}}(\omega)]$ (shown by the solid curve), between the (c) top valance state at ▲ and the bottom conduction state at ● and (d) the bottom conduction state at ▲. See Fig. 2 for the symbols. The shaded regions are the Eliashberg function of the valence (red) and conduction (green) states. (e) Excitonic Elishberg function showing the strength of the exciton-phonon couplings of the lowest bright exciton at different temperatures.

● Fig. 5(b)], we observe a redshift of about 67 meV at 0 K, resulting in a total shrinkage of 73 meV from the bare direct gap. Similarly, for the conduction state at ▲, the redshift is approximately 85 meV, leading to a 91 meV indirect zero-point renormalization. The valence band spectrum show a blueshift at 0 K. However, with an increase in temperature, the spectrum initially redshift and then blueshift. In contrast, the conduction spectra consistently redshift within the stated temperature range. Consequently, the overall gap shrinkage in this case depends on the rate of redshifting of the conduction states (see Fig. 6). In effect, this gap reduction is also warranted through the electronic Eliashberg functions discussed below. Nevertheless, these ZPM are quite large when compared to 2D MoS_2 (75 meV) [46] and WSe_2 (31 meV) [48], and we attribute this because of the low atomic masses of boron atoms which tends to vibrate more in the CP1 primitive cell.

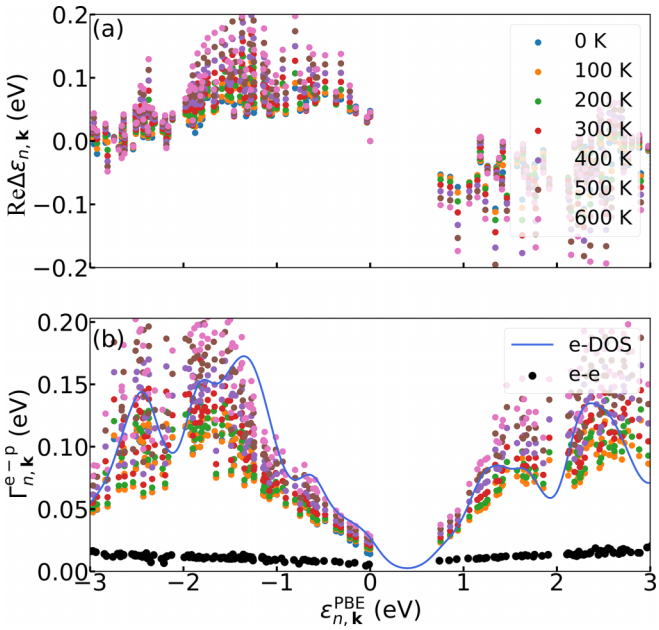

FIG. 4. (a) Corrections from Fan+DW energies at different temperatures. (b) Phonon mediated electronic linewidths at different temperatures. The solid curve is the electronic DOS (scaled to fit). The black dots are the linewidths (scaled) from *GW* corrections.

Figures 3(c) and 3(d) represents the real part of the complex electronic Eliashberg function [44] $g^2F_{n\mathbf{k}}(\omega) = \sum_{\mathbf{q}\nu} \frac{\partial \varepsilon_{n\mathbf{k}}}{\partial n_B(\omega_{\mathbf{q}\nu})} \delta(\omega - \omega_{\mathbf{q}\nu})$ evaluated at several specific points in the electronic dispersion, such as VBM, CBM, etc., shown by symbols in Fig. 2. Here, $\varepsilon_{n\mathbf{k}}$ are the renormalized complex electronic energies, n_B is the Bose occupation factor and the sum extends to all phonon momenta $\mathbf{q}$ and modes ν. g and F represent the electron-phonon matrix elements and the phonon-DOS, respectively. Figure 3(c) shows $\mathrm{Re}g^2F_{n\mathbf{k}}(\omega)$ for the valence state at ▲ and conduction state at ●. These are the locations of the direct band gap in the dispersion. We see that the sign of $\mathrm{Re}g^2F_{n\mathbf{k}}(\omega)$ depends on the sign of the real parts of the poles in Fan and DW self-energy equations (see, for example, Ref. [47]). In conventional semiconductors, $\mathrm{Re}g^2F_{n\mathbf{k}}(\omega)$ is positive for valence states and negative for conduction states. Hence, the difference $\mathrm{Re}[g^2F^c_{n\mathbf{k}}(\omega) - g^2F^v_{n\mathbf{k}}(\omega)]$ becomes negative in most cases, thus resulting in a band-gap shrinkage with temperature. Further, as $\omega \to 0$, this difference tends to zero, indicating crystalline translation invariance. We also note that $\mathrm{Re}[g^2F^c_{n\mathbf{k}}(\omega) - g^2F^v_{n\mathbf{k}}(\omega)]$ also tends to zero as ω approaches the Debye frequency limit. We use this justification to understand the temperature-dependent direct band-gap shrinkage as shown in Fig. 6.

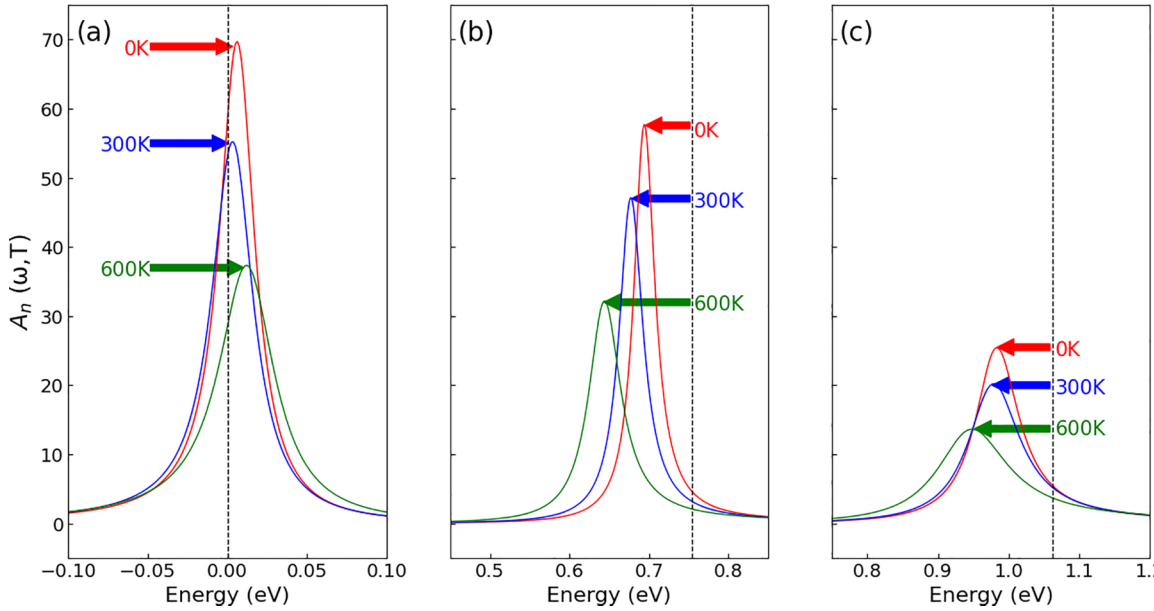

FIG. 5. Spectral function at three different temperatures in the (a) top valence state at ▲ and at conduction states (b) ● and (c) ▲, respectively. Significant shortening as well as broadening of the Lorentzian peaks can be seen as a result of large electron-phonon interaction at high temperatures.

To understand which phonon mode is responsible for the band-gap shrinkage, we look for the peaks of $\mathrm{Re}[g^2F^c_{n\mathbf{k}}(\omega) - g^2F^v_{n\mathbf{k}}(\omega)]$ along ω (which is also apparently proportional to the phonon DOS). We observe that the difference shows major peaks spreading from the midacoustic modes to lower optical modes (350–950 cm^{-1}) in the phonon dispersion and the DOS. Such modes are infected with complicated torsional motions. In the case of a valence state at ▲ and conduction state at ▲ (indirect gap location), we see a similar trend of negative $\mathrm{Re}[g^2F^c_{n\mathbf{k}}(\omega) - g^2F^v_{n\mathbf{k}}(\omega)]$, aiding the gap to shrink with temperature. However, in the lower temperature region, we observe a slight incremental tendency in the indirect gap with temperature. This behavior arises from the relatively slow redshifting of the conduction spectral function. Nevertheless, we cannot entirely discount the possibility of computational noise within this rigorous method [67]. Overall, the same group of phonon modes is responsible for an effective reduction in the gap.

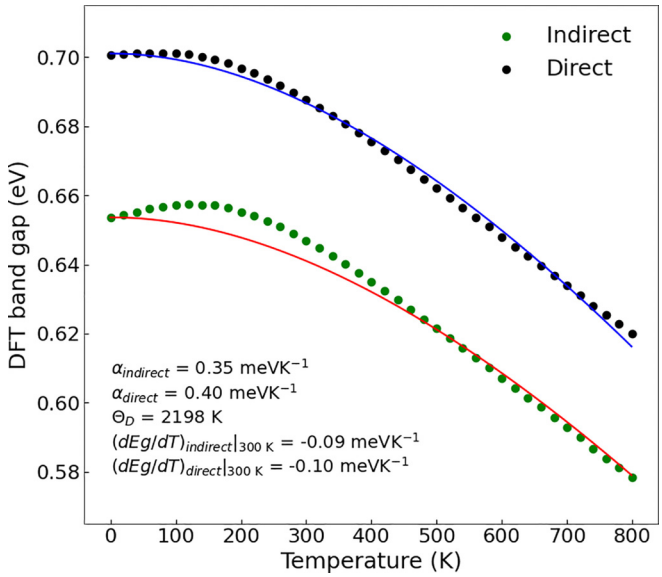

FIG. 6. Temperature dependent band gap variations due to the electron-phonon interactions. The solid line is a fit from Varshni's equation [66]. Dots are the *ab initio* results.

We use the phenomenological Varshni's model [66] $E_g(T) = E_g(0\,\mathrm{K}) - [\frac{\alpha T^2}{\Theta_D + T}]$ as a fit to describe the temperature dependency on the band gap in both cases, where α is material constant and Θ_D is the Debye temperature. We observe that a best fit of the model occurs for α=0.35 and 0.40 meV K^{-1} for the indirect and direct band, respectively. The corresponding slopes near 300 K is about −0.09 and −0.10 meV K^{-1}, respectively. From our *ab initio* calculation, we find the ground state indirect and direct electronic band gaps to be 0.65 eV and 0.70 eV at 0 K, and 0.65 and 0.69 eV at 300 K, respectively.

C. Excited state energies and temperature dependent absorption spectra

The excited state quasiparticle energy correction is shown in Fig. 2. Switching on the Hartree-Fock (HF) electron-electron static correlation opens a direct gap of 4.66 eV [see the HF gap convergence in Fig. S2(a) of the SM]. In the presence of dynamic screening, the quasiparticle correction reduces to about 1.55 eV, leading to a direct gap of 2.34 eV (see Figs. S2(b) and S2(c), respectively, in the SM for related convergences [53]). This quasiparticle gap is situated along the same Γ-**X** route as before and is the location of the fundamental (lowest bound) optical transition. These corrected *GW* excited state energies can now be used to understand the optical transitions.

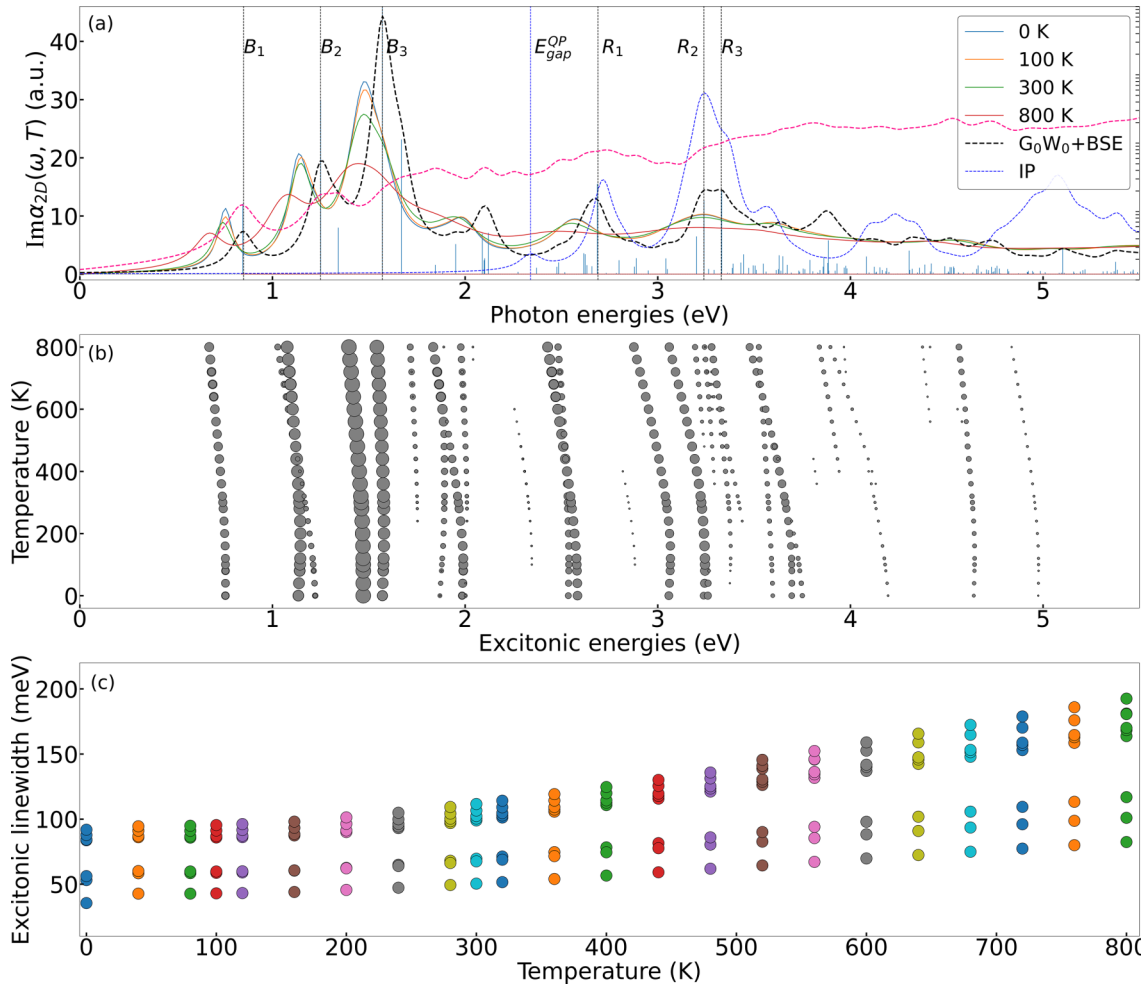

FIG. 7. (a) 2D macroscopic polarizability function from the solution of BSE in case of FA (dashed curve) and temperature-dependent conditions (solid curves). The vertical dotted lines are the FA bound B_1, B_2, B_3 and resonant R_1, R_2, and R_3 excitonic peaks. The vertical solid lines are the FA excitonic oscillator strengths at all transitions. The vertical dashed line exhibits the quasiparticle direct gap $E_{\text{gap}}^{\text{QP}}$. Absorption spectra using the IP approximation at FA condition is also demonstrated to understand the deviation from the BSE. The joint-DOS along the secondary y axis is shown in the same subplot. (b) Exciton oscillator strengths as function of temperature for all exciton energies. Excitons with oscillator strengths more than 20% in this case are considered to be bright. (c) Bound excitonic linewidth (<2 eV and >10% strengths) as function of temperature for all the exciton peaks in absorption spectra.

To account for optical absorption including excitonic effects, we write the BSE as [52,71,72]

$$(\varepsilon_{c\mathbf{k}} - \varepsilon_{v\mathbf{k}})A^s_{vc\mathbf{k}} + \sum_{v'c'\mathbf{k}'} \langle vc\mathbf{k}|\Xi_{vc\mathbf{k},v'c'\mathbf{k}'}|v'c'\mathbf{k}'\rangle A^s_{v'c'\mathbf{k}'} = \mathcal{E}^s_X A^s_{vc\mathbf{k}}, \quad (1)$$

in which v and c are the occupied and unoccupied states, $\varepsilon_{c,v\mathbf{k}}$ are the quasiparticle energies (i.e., *GW* quasiparticle energies on the top of the Kohn-Sham energies), $A^s_{vc\mathbf{k}}$ is obtained by diagonalizing Eq. (1) and is the amplitude of a free exciton in state s with electron and hole state $|c\mathbf{k}\rangle$ and $|v\mathbf{k}\rangle$, respectively. $\mathcal{E}^s_X$ are the exciton energies and Ξ is the electron-hole interaction kernel. We then solve the BSE (see the upper and lower panel of Fig. S3 in the SM for related convergences [53]), first with an FA approximation (in the absence of lattice vibrations) using a small empirically positive constant of 70 meV, corresponding to an FWHM broadening. Figure 7(a) (upper panel) shows the macroscopic polarizability function obtained from the solution of the BSE, which is strictly valid for 2D systems and is proportional to the absorbance [73]. In CP1 borophene, we observe that absorption is primarily governed by three main optical transitions, represented by peaks B_1, B_2, and B_3 at energy positions of 0.85, 1.25, and 1.57 eV, respectively. The lowest bound exciton in the spectrum resides at approximately 0.84 eV and is characterized as a nondegenerate and optically dark state, with a small excitonic oscillator strength. We have determined that excitons B_1 and B_3 consist solely of nondegenerate electron-hole pairs. In contrast, B_2 is identified as a degenerate state featuring a bright-dark pair. All three bright excitons are situated below the continuum, rendering them bound excitons. Conversely, the subsequent three smaller peaks, R_1, R_2, and R_3, are positioned above the continuum, classifying them as having resonant excitonic characteristics. Both R_1 and R_2 are nondegenerate, while R_3 incorporates contributions from a pair of degenerate bright and dark excitons. To show the importance of these correlation, we also show the spectra when the electron-hole kernels

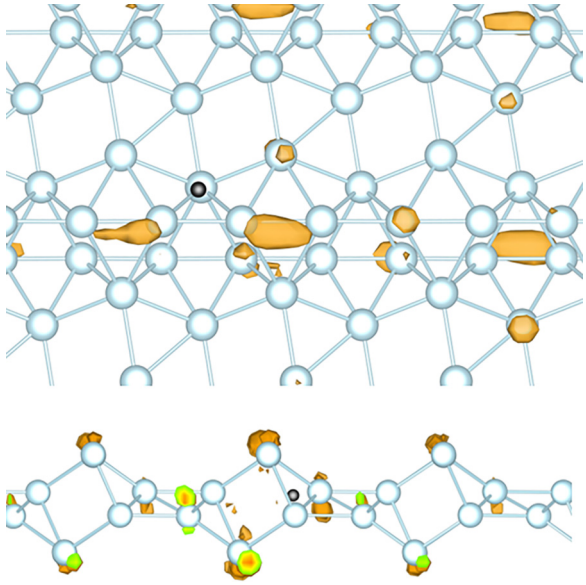

FIG. 8. Excitonic probability distribution function expanded over the real-space lattice. The upper subplot shows the top view, while the bottom is the side view.

are just at the level of Hartree interaction [the so-called independent particle (IP) absorption]. Immediately we see that in the presence of just a Hartree potential, the fundamental peak appears at the onset of the continuum. Since the absorption spectrum does not display any dark states, we have plotted the joint DOS. Upon examination, we observe that the presence of a dark state in proximity to any bright state tends to alter the slope of the joint DOS. It becomes evident that the lowest exciton in the absorption spectra is indeed dark.

Using the excitonic wave function $\Psi^s(\mathbf{r}_e, \mathbf{r}_h) = \sum_{cv\mathbf{k}} A^s_{cv\mathbf{k}} \psi^*_{v\mathbf{k}}(\mathbf{r}_h)\psi_{c\mathbf{k}}(\mathbf{r}_e)$ [where the electron (hole) coordinates are $\mathbf{r}_e$ ($\mathbf{r}_h$)], one can understand about the excitonic character, whether they are Matt-Wannier or Frenkel type. For this, we evaluate $|\Psi^s(\mathbf{r}_e, \mathbf{r}_h)|^2$ and project on the real-space lattice. This would then give the probability of electron localization about a hole when the later is fixed in lattice ($\mathbf{r}_e = \mathbf{r}$ and $\mathbf{r}_h = \bar{\mathbf{r}}_h$). We therefore fix a hole on the top of the boron atom ($\sim$1 Å) within the cell. The probability function for the lowest bound exciton is illustrated in Fig. 8. The in-plane view suggests that the exciton is primarily localized to a few in-plane atoms nearby, indicating that the B_1 exciton exhibits a Frenkel-type character. While the extent of the exciton distribution along the out-of-plane

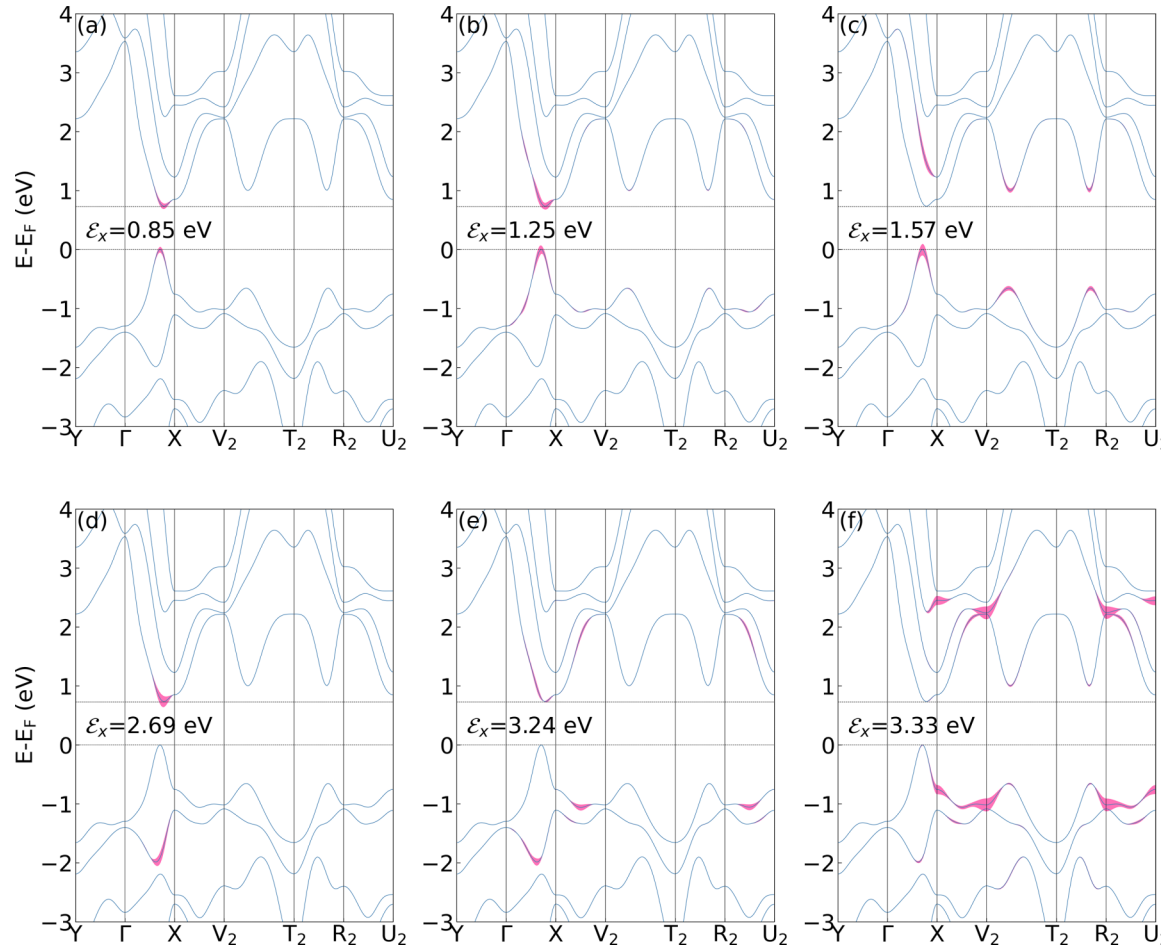

FIG. 9. Optical transitions represented by excitonic weights (square module of the excitonic wave function) for the bound and resonant excitons along the CP1 borophene BZ. The upper panels (a)–(c) are the bound excitons B_1, B_2, and B_3, respectively. The lower panels (d)–(f) are the resonant excitons R_1, R_2, and R_3, respectively. The transitions are shown by the excitonic weights in pink.

direction does not appear to extend far, this suggests that interlayer excitonic interactions may not be significant. Such an effect could reduce the Davydov splitting [74] observed in the absorption spectra. Furthermore, we observe that the distribution function of B_1 does not exhibit any symmetry, reflecting the crystalline asymmetry of CP1. In contrast, B_2 and B_3 are less bound and, as a result, more delocalized along the in-plane directions, giving rise to Mott-Wannier type excitons.

Figure 9 below exhibits all the aforementioned optical transitions for the peaks shown in the absorption spectra. The major bound excitonic transitions at the three consecutive peaks are depicted in the upper panels (a)–(c), respectively. We observe that the B_1 exciton is primarily centered around the quasiparticle direct gap along the Γ-**X** route. In comparison, the other two bound excitons exhibit greater dispersion across the BZ. The resonant excitons are primarily associated with the top two valence bands in the first two cases, and additionally involve the three lowest conduction bands for R_3. To gain insight into the orbital contributions to these excitons, we can refer to Fig. S1 in the SM. For instance, it is evident that all the bound excitons originate from $2p_z$ orbital transitions, while the R_1 and R_2 excitons exhibit significant contributions from $2p_y$ (valence states) transitioning to $2p_z$ (conduction states), respectively. In contrast, the R_3 exciton arises from transitions involving mixed $2p_y$ and $2p_x$ (valence states) orbitals to the $2p_z$ (conduction state).

The absorption spectrum discussed in the preceding paragraph was analyzed under the conditions of the FA approximation. We now consider the lattice vibrations and go beyond the Tamm-Dancoff approximation to include electron-hole pairs and antipairs, as demonstrated by Marini [44]. These corrections cause the single-particle energy state to become a complex quantity and produce their natural nonradiative lifetimes, as given by [44] $\gamma_{\mathrm{NR}}(T) = (2\tau^s_{\mathrm{NR}})^{-1} = \mathrm{Im}\mathcal{E}^s_X(T) = \int d\omega \mathrm{Im}[g^2F_s(\omega,T)][n_B(\omega,T)+\frac{1}{2}]$, in which $g^2F_s(\omega,T) = \sum_{cv}|a^s_{cv}(T)|^2[g^2F_c(\omega) - g^2F_v(\omega)]$ is the exciton-phonon coupling function while the other variables are defined therein. The change in exciton energies are $\mathrm{Re}\Delta\mathcal{E}^s_X(T) = [\langle s(T)|H^{\mathrm{FA}}|s(T)\rangle - \langle s|H^{\mathrm{FA}}|s\rangle] + \int d\omega \mathrm{Re}[g^2F_s(\omega,T)](n_B(\omega,T)+\frac{1}{2})$. The first term represents a coherent contribution through which a phonon interacts with an exciton and modifies its amplitude. The second term represents an incoherent interaction through which a phonon reacts separately with an electron and a hole. These equations categorize the absorption spectra at various temperatures. The effect of zero-point motion can be seen in the 0 K spectra shown in Fig. 7(a). As the temperature goes to 0 K, the Bose number goes to zero, leaving only the $\frac{1}{2}$ factor. This justifies the spectrum due to residual intrinsic spatial quantum uncertainties imposed by Heisenberg's uncertainty principle, which is completely different from the FA situation. We find that at 0 K, the B1 peak redshifts by approximately 97 meV from its corresponding FA location. This shift can be understood based on the sign of the exciton-phonon coupling function $g^2F_s(\omega,T)$. It's worth noting that the sign is positive when $g^2F_c(\omega) > g^2F_v(\omega)$ and negative when $g^2F_c(\omega) < g^2F_v(\omega)$. A positive sign would result in a positive integral area for the incoherent coupling, thereby causing a blueshift or an increase in excitonic energies. Conversely, a negative sign would lead to a negative integral area, resulting in decreased excitonic energies and a redshift. This is particularly shown in Fig. 3(e), where we plot the exciton-phonon coupling function for the lowest exciton B_1 at different temperatures. The integral area is mostly negative in the temperature limit 0–300 K which strongly suggests an intense incoherent exciton-phonon coupling coming from phonon set between 350–950 cm^{-1} with complicated torsional modes.

Now we return to Fig. 7(b), which demonstrates all the excitionic energy behavior with temperatures in the range 0–5 eV. We consider those excitons to be bright, which shows a strength more than 10%. Clearly, we can see the fact that with increasing temperatures many excitons changes their character from optically bright (large oscillator strengths) to optically dark (small oscillator strengths) and vice versa. The oscillator strengths associated with each of these excitons are demonstrated through the size of the circles. However, there are a few, for example, like the lowest bright exciton B_1, which continues to remain bright within this temperature range. Interestingly, we find that this oscillator strength is also exchanged between two excitons. Whenever any two excitons come in close proximity, they tend to share their strength in such a way that a darker one starts becoming bright. This is seen, for example, for the set of excitons near 2 eV. In the case when they depart, the darker starts becoming more bright. This sharing of excitonic character with respect to temperature is also observed in bulk h-BN [44]. We observe that almost all resonant excitons redshift with the increase in temperature. Further, as the temperature increases, the magnitude of the peaks becomes dwarf. The fundamental optical gaps at 0 K and 300 K are found to be 0.76 and 0.74 eV, respectively. Careful inspection also shows that the absorption spectra is also resilient to temperature effects between 0 K to 100 K, exhibiting a slow variation. In effect, the fundamental bound excitonic energies is found to decrease with temperature, similar to other 2D MoS_2 [46], WSe_2 [48], and h-BN [49].

Because of the presence of a finite broadening coming from the electron-phonon renormalization, excitons now acquire a finite homogeneous nonradiative linewidth. No manual broadening is therefore required. The nonradiative linewidth also increases, exhibiting a flattened spectra. Figure 7(c) demonstrates the phonon induced nonradiative linewidth of all such excitons. The dependency on temperature can also be explained from the phenomenological relation [19] $\gamma_{\mathrm{NR}}(T) = \gamma_0 + \gamma_{\mathrm{ac}}T + [\frac{\gamma_{\mathrm{op}}}{\exp(\frac{\Omega}{k_BT})-1}]$, where γ_0 is the broadening at 0 K, γ_{ac} and γ_{op}, respectively, signifies the exciton-acoustic and exciton-optical phonon interaction strengths and Ω denotes the relevant phonon frequency. In the case of the B_1 exciton, we find from our calculations that the broadening at 0 K is almost 36 meV. This is shown in Figs. 10(a) and 10(b). From Fig. 10(c), the linewidth variation is almost linear up to 300 K, signifying an intense exciton-acoustic coupling. As the temperature rises, the phonon number increases, mostly near the midacoustic zone, resulting in a strong interaction as shown in Fig. 10(d). To compare the strengths, we obtain the coupling parameters which best describes our data, with $\omega = 375\ \mathrm{cm}^{-1}$, $\gamma_{\mathrm{op}} = 4.7$ meV, and $\gamma_{\mathrm{ac}} = 38.3\ \mu\mathrm{eV/K}$. The 0 K

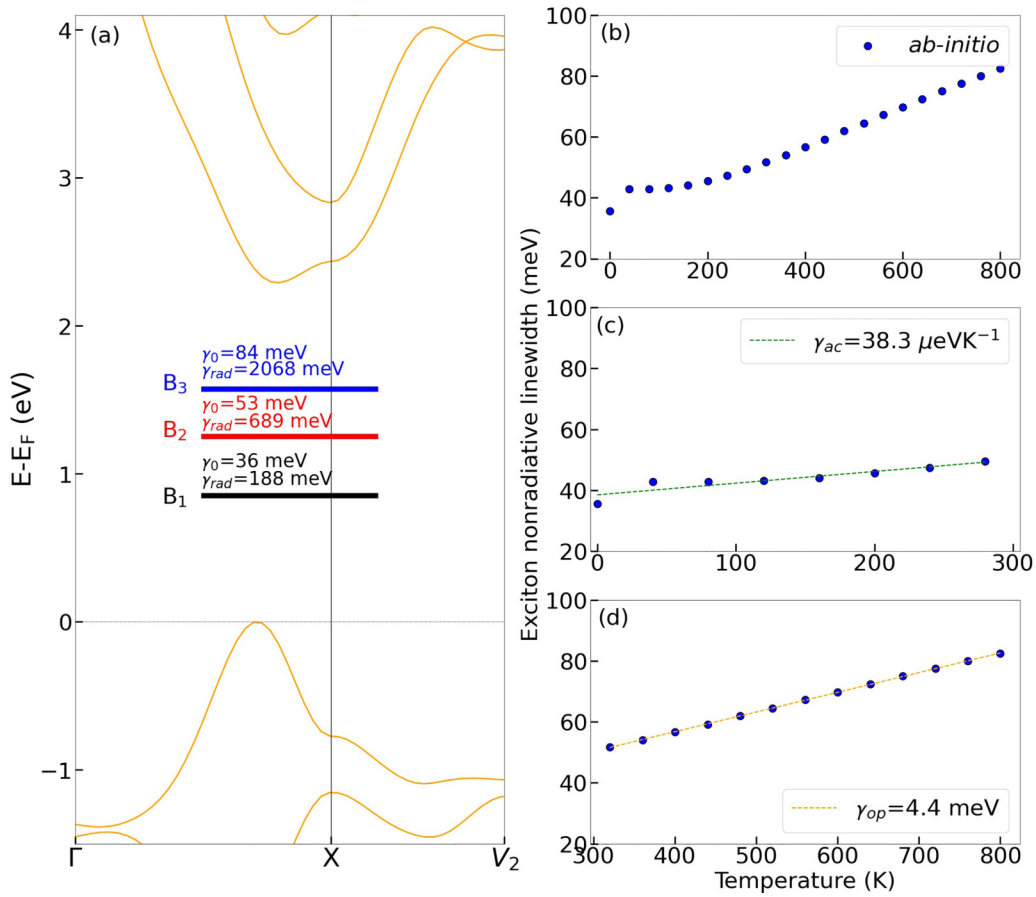

FIG. 10. (a) Exciton energies of the three bound excitons along with their intrinsic radiative and nonradiative linewidths at 0 K in the G_0W_0 dispersion. (b) *Ab initio* nonradiative lifetime of B_1 exciton along with the fits (c) at low and (d) high temperatures.

widths for the other two bound excitons are 53 and 84 meV, respectively. These coupling parameters (summarized in Table II) can be compared to the contemporary 2D materials, for example, MoS_2 (h-BN encapsulated) [20] and WSe_2 (sapphire substrate) [75], where γ_0 at 0 K is reported to 4 ± 0.2 and 1.6 ± 0.3 meV, while γ_{ac} is 70 ± 5 and 60 μeV/K, respectively.

In addition to the nonradiative lifetime, we also report here the intrinsic radiative lifetime. Palummo *et al.* [39] showed that this can be written as $\gamma_R^s(0) = [\tau_R^s(0)]^{-1} = \frac{8\pi e^2 \mathcal{E}^s(0)}{\hbar^2 c} \frac{\mu_s^2}{A_{uc}}$, where $\tau_R^s(0)$ and μ_s^2 are the intrinsic radiative lifetime [whereas $\gamma_R^s(0)$ is the corresponding rate] of the exciton in the state s at the optical dipole limit, and transition dipole square modulus divided by the total discrete momenta sampling, respectively. In addition, c is the speed of light and A_{uc} is the area of the unit cell. We find that the intrinsic radiative lifetimes of the three bright excitons B_1, B_2, B_3 are about 22 fs (188 meV), 6 fs (689 meV), and 2 fs (2068 meV), respectively. The thermally averaged radiative lifetime at low temperature can then be obtained by using a parabolic excitonic dispersion approximation [39] as $\langle \tau_R^s \rangle = \tau_R^s(0) \frac{3}{4} (\frac{\mathcal{E}^s(0)^2}{2M_s c^2})^{-1} k_B T$, in which M_s is the effective exciton mass obtained from the sum of the effective hole and electron masses at the direct gap, respectively. Our calculation shows an effective exciton mass of $0.98m_0$, $0.98m_0$, and $0.87m_0$ for B_1, B_2, and B_3 excitons, respectively, where m_0 is the rest mass of the electron. We estimate the corresponding $\langle \tau_R^s \rangle$ at 300 K to be 0.6, 0.075, and 0.013 ns, respectively.

As the temperature increases, $\langle \tau_R^s \rangle$ decreases for the three consecutive excitons, with slopes of 2, 0.25, and 0.045 ps/K, respectively (see Fig. S5 in the SM). These reduced lifetimes

TABLE II. Excitonic BE and linewidth phenomenological constants of B_1 exciton at room temperature.

Exciton binding energy(eV)	Linewidth (meV)	γ_0 (0 K) (meV)	γ_{ac} (μeV/K)	γ_{op} (meV)	Ω (meV)
1.5	51	36	38.3	4.7	46.5

TABLE III. Excitonic radiative and nonradiative lifetimes in clustered P1 borophene at 0 K and 300 K.

Excitons	τ_{NR} (0 K) (in fs)	τ_{NR} (300 K) (in fs)	τ_R (0 K) (in fs)	$\langle \tau_R \rangle$ (300 K) (in ns)	$\langle \tau_R^{\text{eff}} \rangle$ (300 K) (in ns)
B_1	57	40	22	0.6	1.4
B_2	39	29	6	0.075	0.16
B_3	25	21	2	0.013	0.013

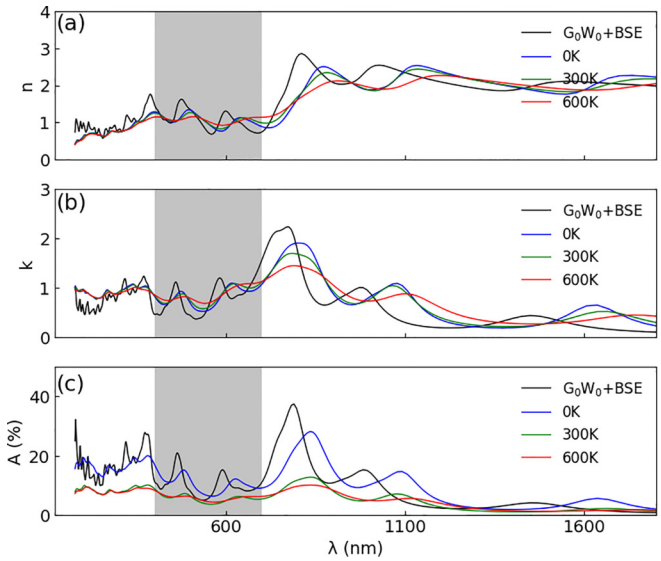

FIG. 11. (a) The refractive index n, (b) extinction coefficient k, and (c) absorbance A as a function of wavelength in the FA condition and various temperatures. The shaded region exhibits the visible spectrum.

lead to an extremely fast recombination process. An effective radiative lifetime, $\langle \tau_R^{\text{eff}} \rangle$, at higher temperatures can also be determined by constructing a weighted average of $\langle \tau_R^s \rangle$ for the lowest energy bright and dark excitons. This approach provides a reasonable match to the experimental RM lifetimes for 2D materials [39].

For comparison, we also present the phonon-assisted nonradiative lifetimes at 300 K, as summarized in Table III. Overall, our analysis finds that nonradiative recombination in CP1 borophene is exceptionally fast compared to the effective radiative recombination processes, on the order of tens of femtoseconds even at 300 K, and is comparable to that of monolayer MoS_2 and WS_2 [19].

To complete the discussion, we use the complex dielectric function to compute the important optical coefficients like refractive index (n), extinction coefficient (k), and the absorbance (A) as a function of wavelength λ both at the frozen atom G_0W_0+BSE level and at three different temperatures in Figs. 11(a)–11(c), respectively. We see that the refractive index varies between 1.3 and 0.8 in the visible region (indicated by a shaded color) whereas the extinction coefficient and absorbance vary between (0.6, 1.1) and (3.62, 8.82)%, respectively, at RT. At long wavelengths, the refractive index tends almost to a value 2.1.

We want to emphasize that our results do not yet incorporate the precise exciton-phonon matrix elements necessary for solving the BSE Hamiltonian, such as highlighted recently by Chen *et al.* [76]. These matrix elements should ideally be integral components of the BSE Hamiltonian rather than relying on electron-phonon couplings and electronic state corrections. Furthermore, including these matrix elements is essential for modeling exciton-phonon scattering along the exciton dispersion and determining their respective mean-free paths, as discussed in Ref. [76]. The development and integration of these elements into the MBPT code are ongoing and currently in the testing phase. Nevertheless, this work effectively captures essential exciton-phonon physics and interaction strengths, as indicated by previous research [44,46–48,65]. We believe that our results provide valuable insights into the optical processes within the clustered semiconducting phase of borophene.

III. CONCLUSIONS

In this paper, we presented a comprehensive theory of optical processes in monolayer CP1 borophene, considering the influence of lattice vibrations. Our findings reveal that electron-phonon correlations introduce significant corrections to the optical absorption spectrum, even at 0 K, and should not be overlooked. We observe that the absorption spectrum is primarily governed by three dominant bound exciton peaks, which remain resilient to temperatures up to 100 K. The collective impact of various couplings, such as electron-electron, electron-hole, electron-phonon, and exciton-phonon interactions, significantly modifies the nonradiative linewidth of the lowest bound exciton to approximately 51 meV at RT, a value similar to that found in the contemporary monolayer TMDC family. These recombination processes are notably faster than the effective radiative processes. We believe that these remarkable results position clustered-P1 borophene as a promising candidate for optoelectronic-based devices.

ACKNOWLEDGMENTS

The paper is supported under Science and Engineering Research Board (SERB)-MATRICS No. MTR/2021/000017 and No. MTR/2019/000047 India. A portion of the calculations were performed at National Supercomputing Mission (NSM) *Param Pravega* and *Param Smriti* at Indian Institute of Science, Bangalore and at Mohali, India, respectively. The authors acknowledge these facilities.

[1] Z. Ye, T. Cao, K. O'Brien, H. Zhu, X. Yin, Y. Wang, S. G. Louie, and X. Zhang, Probing excitonic dark states in single-layer tungsten disulphide, Nature (London) **513**, 214 (2014).

[2] Y. Ye, J. Xiao, H. Wang, Z. Ye, H. Zhu, M. Zhao, Y. Wang, J. Zhao, X. Yin, and X. Zhang, Electrical generation and control of the valley carriers in a monolayer transition metal dichalcogenide, Nat. Nanotechnol. **11**, 598 (2016).

[3] G. Wang, C. Robert, A. Suslu, B. Chen, S. Yang, S. Alamdari, I. C. Gerber, T. Amand, X. Marie, S. Tongay, and B. Urbaszek, Spin-orbit engineering in transition metal dichalcogenide alloy monolayers, Nat. Commun. **6**, 10110 (2015).

[4] K. F. Mak, K. He, J. Shan, and T. F. Heinz, Control of valley polarization in monolayer MoS_2 by optical helicity, Nat. Nanotechnol. **7**, 494 (2012).

[5] A. M. Jones, H. Yu, N. J. Ghimire, S. Wu, G. Aivazian, J. S. Ross, B. Zhao, J. Yan, D. G. Mandrus, D. Xiao, W. Yao, and X. Xu, Optical generation of excitonic valley coherence in monolayer WSe_2, Nat. Nanotechnol. **8**, 634 (2013).

[6] A. Srivastava, M. Sidler, A. V. Allain, A. K. Dominik S. Lembke, and A. Imamoğlu, Valley Zeeman effect in elementary optical excitations of monolayer WSe_2, Nat. Phys. **11**, 141 (2015).

[7] E. Poem, Y. Kodriano, C. Tradonsky, N. H. Lindner, B. D. Gerardot, P. M. Petroff, and D. Gershoni, Accessing the dark exciton with light, Nat. Phys. **6**, 993 (2010).

[8] T. Mueller and E. Malic, Exciton physics and device application of two-dimensional transition metal dichalcogenide semiconductors, npj 2D Mater. Appl. **2**, 29 (2018).

[9] G. Wang, A. Chernikov, M. M. Glazov, T. F. Heinz, X. Marie, T. Amand, and B. Urbaszek, *Colloquium*: Excitons in atomically thin transition metal dichalcogenides, Rev. Mod. Phys. **90**, 021001 (2018).

[10] K. He, N. Kumar, L. Zhao, Z. Wang, K. F. Mak, H. Zhao, and J. Shan, Tightly bound excitons in monolayer WSe_2, Phys. Rev. Lett. **113**, 026803 (2014).

[11] D. Le, A. Barinov, E. Preciado, M. Isarraraz, I. Tanabe, T. Komesu, C. Troha, L. Bartels, T. S. Rahman, and P. A. Dowben, Spin-orbit coupling in the band structure of monolayer WSe_2, J. Phys.: Condens. Matter **27**, 182201 (2015).

[12] K. Kim, J.-U. Lee, D. Nam, and H. Cheong, Davydov splitting and excitonic resonance effects in Raman spectra of few-layer $MoSe_2$, ACS Nano **10**, 8113 (2016).

[13] A. T. Hanbicki, M. Currie, G. Kioseoglou, A. L. Friedman, and B. T. Jonker, Measurement of high exciton binding energy in the monolayer transition-metal dichalcogenides WS_2 and WSe_2, Solid State Commun. **203**, 16 (2015).

[14] A. F. Rigosi, H. M. Hill, K. T. Rim, G. W. Flynn, and T. F. Heinz, Electronic band gaps and exciton binding energies in monolayer $Mo_xW_{1-x}S_2$ transition metal dichalcogenide alloys probed by scanning tunneling and optical spectroscopy, Phys. Rev. B **94**, 075440 (2016).

[15] B. Zhu, X. Chen, and X. Cui, Exciton binding energy of monolayer WS_2, Sci. Rep. **5**, 9218 (2015).

[16] G. Zhang, A. Chaves, S. Huang, F. Wang, Q. Xing, T. Low, and H. Yan, Determination of layer-dependent exciton binding energies in few-layer black phosphorus, Sci. Adv. **4**, e9977 (2018).

[17] C. Elias, P. Valvin, T. Pelini, A. Summerfield, C. J. Mellor, T. S. Cheng, L. Eaves, C. T. Foxon, P. H. Beton, S. V. Novikov *et al.*, Direct band-gap crossover in epitaxial monolayer boron nitride, Nat. Commun. **10**, 2639 (2019).

[18] A. Arora, M. Koperski, K. Nogajewski, J. Marcus, C. Faugerasa, and M. Potemski, Excitonic resonances in thin films of WSe_2: From monolayer to bulk material, Nanoscale **7**, 10421 (2015).

[19] M. Selig, G. Berghäuser, A. Raja, P. Nagler, C. Schüller, T. F. Heinz, T. Korn, A. Chernikov, E. Malic, and A. Knorr, Excitonic linewidth and coherence lifetime in monolayer transition metal dichalcogenides, Nat. Commun. **7**, 13279 (2016).

[20] F. Cadiz, E. Courtade, C. Robert, G. Wang, Y. Shen, H. Cai, T. Taniguchi, K. Watanabe, H. Carrere, D. Lagarde, M. Manca, T. Amand, P. Renucci, S. Tongay, X. Marie, and B. Urbaszek, Excitonic linewidth approaching the homogeneous limit in MoS_2-based van der Waals heterostructures, Phys. Rev. X **7**, 021026 (2017).

[21] W. Pacuski, M. Grzeszczyk, K. Nogajewski, A. Bogucki, K. Oreszczuk, J. Kucharek, K. E. Połczyńska, B. Seredyński, A. Rodek, R. Bożek *et al.*, Narrow excitonic lines and large-scale homogeneity of transition-metal dichalcogenide monolayers grown by molecular beam epitaxy on hexagonal boron nitride, Nano Lett. **20**, 3058 (2020).

[22] L. Guo, C.-A. Chen, Z. Zhang, D. M. Monahan, Y.-H. Lee, and G. R. Fleming, Lineshape characterization of excitons in monolayer WS_2 by two-dimensional electronic spectroscopy, Nanoscale Adv. **2**, 2333 (2020).

[23] I. Boustani, Systematic *ab initio* investigation of bare boron clusters: Determination of the geometry and electronic structures of B_n ($n = 2 - 14$), Phys. Rev. B **55**, 16426 (1997).

[24] A. J. Mannix, X.-F. Zhou, B. Kiraly, J. D. Wood, D. Alducin, B. D. Myers, X. Liu, B. L. Fisher, U. Santiago, J. R. Guest *et al.*, Synthesis of borophenes: Anisotropic, two-dimensional boron polymorphs, Science **350**, 1513 (2015).

[25] B. Feng, J. Zhang, Q. Zhong, W. Li, S. Li, H. Li, P. Cheng, S. Meng, L. Chen, and K. Wu, Experimental realization of two-dimensional boron sheets, Nat. Chem. **8**, 563 (2016).

[26] W. Li, L. Kong, C. Chen, J. Gou, S. Sheng, W. Zhang, H. Li, L. Chen, P. Cheng, and K. Wu, Experimental realization of honeycomb borophene, Sci. Bull. **63**, 282 (2018).

[27] E. S. Penev, S. Bhowmick, A. Sadrzadeh, and B. I. Yakobson, Polymorphism of two-dimensional boron, Nano Lett. **12**, 2441 (2012).

[28] X. Zhang, J. Hu, Y. Cheng, H. Y. Yang, Y. Yao, and S. A. Yang, Borophene as an extremely high capacity electrode material for Li-ion and Na-ion batteries, Nanoscale **8**, 15340 (2016).

[29] C. Zhan, P. Zhang, S. Dai, and D. Jiang, Boron supercapacitors, ACS Energy Lett. **1**, 1241 (2016).

[30] V. Vishnubhotla, A. Kabiraj, A. J. Bhattacharyya, and S. Mahapatra, Global minima search for sodium- and magnesium-adsorbed polymorphic borophene, J. Phys. Chem. C **126**, 8605 (2022).

[31] H. Lin, H. Shi, Z. Wang, Y. Mu, S. Li, J. Zhao, J. Guo, B. Yang, Z.-S. Wu, and F. Liu, Scalable production of free-standing few-layer β_{12}-borophene single crystalline sheets as efficient electrocatalysts for lithium-sulfur batteries, ACS Nano **15**, 17327 (2021).

[32] Q. Li, M. Rellán-Piñeiro, N. Almora-Barrios, M. Garcia-Ratés, I. N. Remediakis, and N. López, Shape control in concave metal nanoparticles by etching, Nanoscale **9**, 13089 (2017).

[33] V. Shukla, J. Wärnå, N. K. Jena, A. Grigoriev, and R. Ahuja, Toward the realization of 2D borophene based gas sensor, J. Phys. Chem. C **121**, 26869 (2017).

[34] C. Hou, G. Tai, Y. Liu, Z. Wu, Z. Wua, and X. Lianga, Ultrasensitive humidity sensing and the multifunctional applications of borophene-MoS_2 heterostructures, J. Mater. Chem. A **9**, 13100 (2021).

[35] S. Guha, A. Kabiraj, and S. Mahapatra, Discovery of clustered-P1 borophene and its application as the lightest high-performance transistor, ACS Appl. Mater. Interfaces **15**, 3182 (2023).

[36] B. Arnaud, S. Lebègue, P. Rabiller, and M. Alouani, Huge excitonic effects in layered hexagonal boron nitride, Phys. Rev. Lett. **96**, 026402 (2006).

[37] A. Ramasubramaniam, Large excitonic effects in monolayers of molybdenum and tungsten dichalcogenides, Phys. Rev. B **86**, 115409 (2012).

[38] X. Wang, A. M. Jones, K. L. Seyler, V. Tran, Y. Jia, H. Zhao, H. Wang, L. Yang, X. Xu, and F. Xia, Highly anisotropic and robust excitons in monolayer black phosphorus, Nat. Nanotechnol. **10**, 517 (2015).

[39] M. Palummo, M. Bernardi, and J. C. Grossman, Exciton radiative lifetimes in two-dimensional transition metal dichalcogenides, Nano Lett. **15**, 2794 (2015).

[40] J. P. Echeverry, B. Urbaszek, T. Amand, X. Marie, and I. C. Gerber, Splitting between bright and dark excitons in transition metal dichalcogenide monolayers, Phys. Rev. B **93**, 121107(R) (2016).

[41] T. Biswas and A. K. Singh, Excitonic effects in absorption spectra of carbon dioxide reduction photocatalysts, npj Comput. Mater. **7**, 189 (2021).

[42] A. Rasmussen, T. Deilmann, and K. S. Thygesen, Towards fully automatized *GW* band structure calculations: What we can learn from 60.000 self-energy evaluations, npj Comput. Mater. **7**, 22 (2021).

[43] M. Dubecký, F. Karlický, S. Minárik, and L. Mitas, Fundamental gap of fluorographene by many-body *GW* and fixed-node diffusion Monte Carlo methods, J. Chem. Phys. **153**, 184706 (2020).

[44] A. Marini, *Ab initio* finite-temperature excitons, Phys. Rev. Lett. **101**, 106405 (2008).

[45] E. Cannuccia and A. Marini, Zero point motion effect on the electronic properties of diamond, trans-polyacetylene and polyethylene, Eur. Phys. J. B **85**, 320 (2012).

[46] A. Molina-Sànchez, M. Palummo, A. Marini, and L. Wirtz, Temperature-dependent excitonic effects in the optical properties of single-layer MoS_2, Phys. Rev. B **93**, 155435 (2016).

[47] E. Cannuccia, B. Monserrat, and C. Attaccalite, Theory of phonon-assisted luminescence in solids: Application to hexagonal boron nitride, Phys. Rev. B **99**, 081109(R) (2019).

[48] H. Mishra, A. Bose, A. Dhar, and S. Bhattacharya, Exciton-phonon coupling and band-gap renormalization in monolayer WSe_2, Phys. Rev. B **98**, 045143 (2018).

[49] H. Mishra and S. Bhattacharya, Giant exciton-phonon coupling and zero-point renormalization in hexagonal monolayer boron nitride, Phys. Rev. B **99**, 165201 (2019).

[50] M. Kolos, L. Cigarini, R. Verma, F. Karlický, and S. Bhattacharya, Giant linear and nonlinear excitonic responses in an atomically thin indirect semiconductor nitrogen phosphide, J. Phys. Chem. C **125**, 12738 (2021).

[51] M. Kolos, R. Verma, F. Karlický, and S. Bhattacharya, Large exciton-driven linear and nonlinear optical processes in monolayers of nitrogen arsenide and nitrogen antimonide, J. Phys. Chem. C **126**, 14931 (2022).

[52] G. Onida, L. Reining, and A. Rubio, Electronic excitations: Density-functional versus many-body Green's-function approaches, Rev. Mod. Phys. **74**, 601 (2002).

[53] See Supplemental Material at http://link.aps.org/supplemental/10.1103/PhysRevB.108.245107 for necessary convergence and supporting figures. A detailed theory on Hedin's *GW* method is discussed in Ref. [54]. A truncated Coulomb potential technique [55] in the *ab initio* Yambo code [56] is used to reduce the effect of repititive periodic images in *GW* calculations. Additionally, a plasmon-pole approximation by Godby and Needs [57] is used to reduce the compuattaional load in computing the screening integral.

[54] F. Aryasetiawan and O. Gunnarsson, The *GW* method, Rep. Prog. Phys. **61**, 237 (1998).

[55] C. A. Rozzi, D. Varsano, A. Marini, E. K. U. Gross, and A. Rubio, Exact Coulomb cutoff technique for supercell calculations, Phys. Rev. B **73**, 205119 (2006).

[56] D. Sangalli, A. Ferretti, H. Miranda, C. Attaccalite, I. Marri, E. Cannuccia, P. Melo, M. Marsili, F. Paleari, A. Marrazzo *et al.*, Many-body perturbation theory calculations using the Yambo code, J. Phys.: Condens. Matter **31**, 325902 (2019).

[57] R. W. Godby and R. J. Needs, Metal-insulator transition in Kohn-Sham theory and quasiparticle theory, Phys. Rev. Lett. **62**, 1169 (1989).

[58] P. Giannozzi, O. Andreussi, T. Brumme, O. Bunau, M. B. Nardelli, M. Calandra, R. Car, C. Cavazzoni, D. Ceresoli, M. Cococcioni *et al.*, Advanced capabilities for materials modelling with Quantum ESPRESSO, J. Phys.: Condens. Matter **29**, 465901 (2017).

[59] P. B. Allen and V. Heine, Theory of the temperature dependence of electronic band structures, J. Phys. C: Solid State Phys. **9**, 2305 (1976).

[60] P. B. Allen and M. Cardona, Temperature dependence of the direct gap of Si and Ge, Phys. Rev. B **27**, 4760 (1983).

[61] H. Y. Fan, Temperature dependence of the energy gap in monatomic semiconductors, Phys. Rev. **78**, 808 (1950).

[62] F. Giustino, S. G. Louie, and M. L. Cohen, Electron-phonon renormalization of the direct band gap of diamond, Phys. Rev. Lett. **105**, 265501 (2010).

[63] G. Antonius, S. Poncé, P. Boulanger, M. Côté, and X. Gonze, Many-body effects on the zero-point renormalization of the band structure, Phys. Rev. Lett. **112**, 215501 (2014).

[64] G. Antonius, S. Poncé, E. Lantagne-Hurtubise, G. Auclair, X. Gonze, and M. Côté, Dynamical and anharmonic effects on the electron-phonon coupling and the zero-point renormalization of the electronic structure, Phys. Rev. B **92**, 085137 (2015).

[65] T. Shen, X.-W. Zhang, H. Shang, M.-Y. Zhang, X. Wang, E.-G. Wang, H. Jiang, and X.-Z. Li, Influence of high-energy local orbitals and electron-phonon interactions on the band gaps and optical absorption spectra of hexagonal boron nitride, Phys. Rev. B **102**, 045117 (2020).

[66] Y. P. Varshni, Temperature dependence of the energy gap in semiconductors, Physica **34**, 149 (1967).

[67] To obtain the complex energies $\varepsilon_{n\mathbf{k}}$ from first principles using norm-conserving pseudopotentials [68], we use the density functional perturbation theory to evaluate the first-order Fan [61] and second-order DW [69] electron-phonon coupling matrices. First, a self-consistent charge density on these regular grid is obtained followed by its first-order derivative with respect to the atomic displacements. A non-self-consistent calculation on these grids was done to evaluate the scattering states with momenta $\mathbf{k}$ to $\mathbf{k}\pm\mathbf{q}$. As the DFPT does not compute the second derivative of the self-consistent charge density, therefore the second order DW matrix elements are constructed by making use of the translational invariance of the crystal in the code Yambo [56]. The second-order DW elements are now transformed similar to the first-order productlike Fan terms. A Sternheimer's [70] method is, in principle, used to compute the sum of over empty states to obtain the corresponding

self-energies. Unfortunately, Yambo does not use Sternheimer's method, due to which the zero-point renormalization (ZPR) converges slowly with the number of empty states (see Fig. S4 in the SM for convergence [53]).

[68] D. R. Hamann, Optimized norm-conserving Vanderbilt pseudopotentials, Phys. Rev. B **88**, 085117 (2013).

[69] E. Cannuccia and A. Marini, Ab-initio study of the effects induced by the electron-phonon scattering in carbon based nanostructures, arXiv:1304.0072.

[70] R. M. Sternheimer, Electronic polarizabilities of ions from the Hartree-Fock wave functions, Phys. Rev. **96**, 951 (1954).

[71] G. Strinati, Dynamical shift and broadening of core excitons in semiconductors, Phys. Rev. Lett. **49**, 1519 (1982).

[72] M. Rohlfing and S. G. Louie, Electron-hole excitations and optical spectra from first principles, Phys. Rev. B **62**, 4927 (2000).

[73] P. Cudazzo, I. V. Tokatly, and A. Rubio, Dielectric screening in two-dimensional insulators: Implications for excitonic and impurity states in graphane, Phys. Rev. B **84**, 085406 (2011).

[74] F. Paleari, T. Galvani, H. Amara, F. Duçastelle, A. Molina-Sánchez, and L. Wirtz, Excitons in few-layer hexagonal boron nitride: Davydov splitting and surface localization, 2D Mater. **5**, 045017 (2018).

[75] G. Moody, C. K. Dass, K. Hao, C.-H. Chen, L.-J. Li, A. Singh, K. Tran, G. Clark, X. Xu, G. Berghaüser *et al.*, Intrinsic homogeneous linewidth and broadening mechanisms of excitons in monolayer transition metal dichalcogenides, Nat. Commun. **6**, 8315 (2015).

[76] H.-Y. Chen, D. Sangalli, and M. Bernardi, Exciton-phonon interaction and relaxation times from first principles, Phys. Rev. Lett. **125**, 107401 (2020).